Comparison of e-NVH Performance of Different PMSMs in Electric Vehicle Powertrain

Comparison of e-NVH Performance of Different PMSMs in Electric Vehicle Powertrain

Simone Ferrari
Energy Department "Galileo Ferraris"
Politecnico di Torino
Turin, Italy
simone.ferrari@polito.it

Luca Ciravegna
Dept. of Mechanical and Aerospace Eng.
Politecnico di Torino
Turin, Italy
luca.ciravegna@polito.it

Giorgio De Donno
Dept. of Mechanical and Aerospace Eng.
Politecnico di Torino
Turin, Italy
giorgio.dedonno@polito.it

Enrico Galvagno
Dept. of Mechanical and Aerospace Eng.
Politecnico di Torino
Turin, Italy
enrico.galvagno@polito.it

Matteo Iannone
D&E Hexagon
Manufacturing Intelligence
Genoa, Italy
matteo.iannone@hexagon.com

Gianmario Pellegrino
Energy Department "Galileo Ferraris"
Politecnico di Torino
Turin, Italy
gianmario.pellegrino@polito.it

***Abstract*—The Noise, Vibration and Harshness (NVH) performance of an electric motor is a crucial aspect in the design and analysis of an electric powertrain. Different motor solutions can lead to different NVH figures, since the fundamental frequency of the NVH sources is intimately related to the motor type and geometry. Moreover, the NVH performance of a powertrain is related to the entire drive train and not just the electric motor. For this reason, two electric motors for traction application are compared in terms of both electromagnetic and NVH performance, considering the complete driveline. Furthermore, a review on the computation of electromagnetic forces at the base of the electric-induced NVH (e-NVH) problem is reported.**

***Index Terms*—Electric Motor, NVH analysis, Traction Electric Motor**

I. Introduction

In recent years, the growth of electrical vehicle push the research on the design and optimization of electric motors and inverters, to be adopted for traction purposes. In the first instance, the designers focused on pure electromechanical performance and efficiency. However, in the last years, the aspect of Noise, Vibration and Harshness (NVH) performance becomes more and more important [1], [2], [3], aiming of a higher comfort of the passengers. Replacing the internal combustion engine with an e-drive unit removed the masking noise from it, highlighting all secondary noises such as those coming from the gearbox and adding new ones, as the electromagnetic tonal ones [4]. There are several sources of vibrations in electrical vehicles [5] and the electromagnetic forces (radial and tangential forces acting on the stator teeth and torque ripple) are the one of interest in the following. For the electromagnetic-induced NVH (e-NVH) problem, the electric motor acts as the source of vibrations, but to capture the system response it is necessary to consider the complete electromechanical system [6]. In this paper, the NVH problem is considered at e-powertrain level, assuming a single-gear ratio gearbox and comparing two different traction e-motors. Before the comparison, the analysis flowchart and the computation are reviewed, with a focus on the NVH sources computation by means of Finite Element Analysis (FEA). Furthermore, the two motors are compared in terms of NVH sources and vibroacoustic response.

II. Electric Powertrain Model

The target application is a 50 kW, 120 Nm curve, with a maximum speed of 12000 rpm. Besides the torque-speed domain, the NVH analysis will be focused on some critical operating points, that are indicated in the folliwing figures. The first point, labeled as *avg* refers to an average situation for NVH analysis, so average speed and relatively low torque, close to the average point of a hypothetical driving cycle. The second, third and fourth points lie on the constant speed characteristic at 50, 90 and 130 km/h. The last test point is the peak torque at base speed. The first 4 test points are typically operating conditions kept for long period from the motor, while the last point is not steady-state operative points, so less important from a NVH analysis. Furthermore, an extended analysis at constant torque and complete range of speed will be also conducted.

A. Electric Motors Selection

For comparison purposes, two electric motors are selected from scientific literature [7], [8], having common target electromagnetic performance figures, in order to ease the comparison. The ratings of the two benchmark motors are reported in Table. I, while their cross-sections are shown in Fig. 1.

The two motors have the same number of pole pairs p and the same ratings (compatible with the selected application), simplifying the comparison and providing a common base for the two candidates. Dealing with the motor structure, the first benchmark is an Interior Permanent Magnet (IPM) motor with Distributed Windings (DW), while the second benchmark is a Surface-mounted Permanent Magnet (SPM) motor with Concentrated Windings (CW).

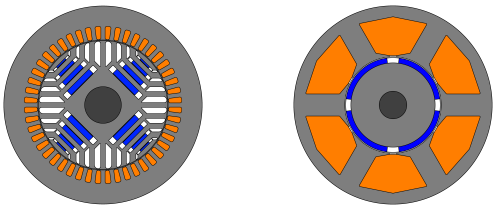

(a) (b)

Fig. 1. Cross sections of the two benchmark motors: a) DW-IPM and b) CW-SPM

		DW-IPM	CW-SPM
Reference		[7]	[8]
Stator outer diameter	(mm)	216	216
Rotor diameter	(mm)	104.4	103
Stack length	(mm)	170	170
Number of pole pairs		2	2
Number of stator slots		48	6
Rated torque	(Nm)	120	120
Base speed	(rpm)	4000	4000
Rated power	(kW)	50	50
Maximum speed	(rpm)	12000	12000
DC link voltage	(Vdc)	300	300
Peak phase current	(Apk)	360	360

TABLE I
SPEC. OF THE TWO BENCHMARK MOTORS.

B. e-Powertrain Model

The e-powertrain gearbox is assumed the same for the two selected e-motors, making a common base for the comparison of the two structures. The powertrain is modeled in Romax [9] and a dual-stage single-speed transmission is chosen as reference. It has an overall transmission ratio of 9 and it is taken from the *Romax* tutorials [10]. Furthermore, the models of the electric motors were defined with a parametric geometry of the components, using the Electric Machine Modeling tool in the software. A representation of the gearbox with and without the housing is reported in Fig. 2.

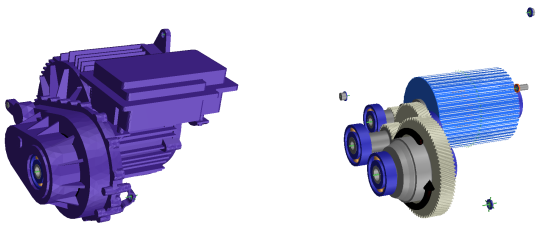

(a) (b)

Fig. 2. e-Powertrain Romax model

III. E-NVH Sources Computation and Comparison

The electromagnetic analysis is performed in SyR-e [11], so the two benchmark motors are imported in this environment and FEA simulations are performed to compute the electromagnetic performance.

A. Electromagnetic Computations

The first comparison between the two motor is done in the electromagnetic environment. The flux and loss maps of the two motors are computed with a PM temperature of 100°C. Then, the efficiency maps are computed with the inverter limits reported in Tab. I and the winding temperature set to 120°C. Further details on the efficiency maps computation are reported in [12]. The efficiency maps of the two motors are shown and compared in Fig. 3, with the curve of the target application reported with black dashed line and the NVH test points highlighted in red.

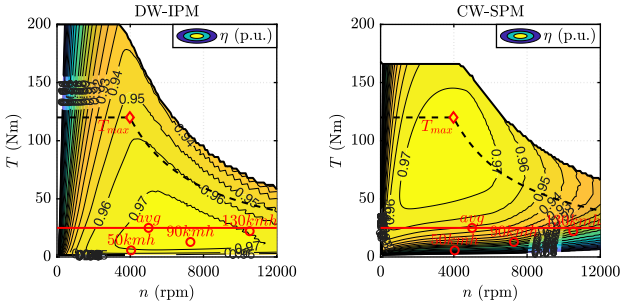

(a) (b)

Fig. 3. Efficiency maps of the two considered motors at $\Theta_{Cu} = 120°\text{C}$ and $\Theta_{PM} = 100°\text{C}$

First of all, it is worth noting that the two motors can easily fulfill the target application, as expected from [7] and [8]. Dealing with the differences, the DW-IPM motor presents a high-efficiency area in the low torque / medium-high speed region, where the NVH test points lays. Conversely, the CW-SPM motor present high efficiency in the low speed / mid-high torque, as expected for this kind of motor, that presents a less efficient field-weakening operation.

During the computation of the efficiency maps, the control trajectories are identified to maximize the motor efficiency. These, together with the flux and torque maps in the (i_d, i_q) domain, can be exploited to compute the peak-to-peak torque ripple ΔT_{pp} over the (T, n) domain, that is reported in Fig. 4 for both motors.

This analysis offers an interesting, even if partial, point of view on the NVH problem. On one side, the torque ripple of the DW-IPM motor increases almost proportionally with the torque level, with higher values in the field-weakening region. Conversely, the CW-SPM motor has more irregular ΔT_{pp} contours, with a minimum region at medium speed and low-medium torque. The different ΔT_{pp} contours shapes reflect in the motor NVH performance, as will be demonstrated later. In details, the DW-IPM motor will have lower peak-to-peak torque ripple for almost all the NVH test points, except the T_{max} point, where the torque ripple of the CW-SPM will be drastically lower (about 40% lower), as also expected from this (T, n) analysis.

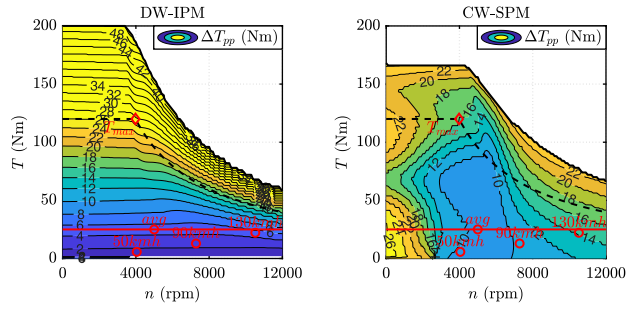

Fig. 4. Peak-to-peak torque ripple maps of the two considered motors at $\Theta_{Cu} = 120°$C and $\Theta_{PM} = 100°$C

One of the crucial points evident in Fig. 4 is the complex relation between torque and torque ripple. This can be partially explained by looking at the torque ripple map in the (i_d, i_q) domain, that are reported in Fig. 5 for the two benchmark motors.

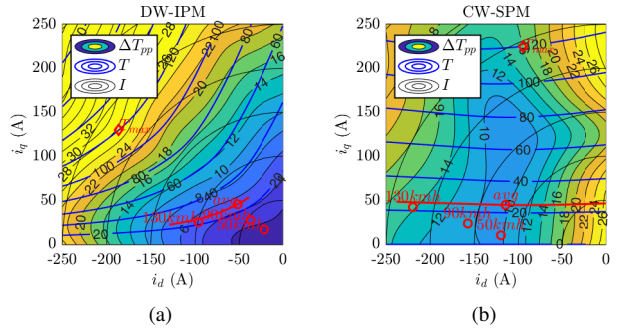

Fig. 5. Peak-to-peak torque ripple maps of the two considered motors at $\Theta_{PM} = 100°$C in the (i_d, i_q) domain.

Looking at the (i_d, i_q) planes, the DW-IPM motor torque ripple increase almost with the current, with a more critical behavior along the $-d$ axis, where the current is used just for field-weakening and the harmonic content increase. The NVH points are reached with lower current, compared to the CW-SPM motor, resulting in higher efficiency (especially at high speed) and lower torque ripple. On the other hand, the CW-SPM motor must spend more current to reach high speed operation and perform field weakening control, in a less efficient way. Its torque ripple contours are less regular than the DW-IPM motor, with a minimum area around -120 A along the d axis and extended along the q axis. This irregular behavior could be caused by the higher PM flux linkage and the peculiar stator-rotor magnetic coupling.

IV. E-NVH Sources

The analysis performed with the (T, n) and (i_d, i_q) planes can give some insights to the NVH performance of the motor, but lack of the frequency information. To better assess the difference between the two motors and to feed the NVH analysis in Romax, the NVH test points are better investigated, performing dedicated simulations to compute torque, radial and tangential tooth waveform function of the rotor position. The analysis is performed also for several points along the $T = 25$ Nm curve, but are not reported here for brevity.

A. Simulation Flowchart and Data Elaboration

The e-NVH sources are computed using the SyR-e environment and FEMM FEA software [13]. For each operating point, identified by the dq currents components extracted from the efficiency maps, a single and detailed simulation is performed to compute all the information needed for the NVH sources. To reduce the computational burden, the FEA simulation is performed on a rotor rotation of 180 electrical degrees and 90 rotor positions, exploiting the symmetry condition. For each rotor position, the torque is extracted directly from FEMM, building the torque waveform. In addition, the radial and tangential magnetic pressure acting on a line close to the stator bore diameter are extracted. At the end of the FEA simulation, the results are: one vector, representing the torque waveform for half electric period rotation and two matrices that represent the radial and tangential magnetic pressure along the airgap of the simulated geometry (one or two poles, based on the machine geometric periodicity) for a rotor rotation of half electrical period.

Then, the dedicated elaboration routine implemented in SyR-e extends the simulated waveform to one electrical period rotation and to the whole airgap circumference (for the magnetic pressures).

Dealing with torque waveform, the extension to the whole electrical period rotation is quite easy and it is displayed in Fig. 6. The black points represents the torque results for each rotor position, while the blue waveform is the complete waveform. The extension to the whole period is done by replicating the torque vector for the rotor position from 180 to 360 electrical degrees.

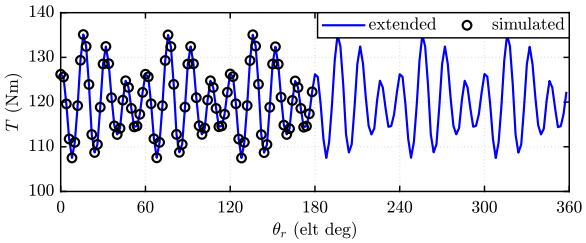

Fig. 6. Torque waveform of DW-IPM motor in the T_{max} point: complete waveform in blue and FEA-simulated points in black.

Dealing with the magnetic pressure at the airgap (needed to compute the force), the process is slightly more complex, since the waveform of radial and tangential magnetic pressure along the airgap is extracted for each rotor position. The complete radial pressure map $p_r(\theta_r, \theta_{gap})$ for the DW-IPM motor in the T_{max} operating point is reported in Fig. 7a for reference. The portion of the map included in the black dashed rectangle are the results from the FEA simulation, while the rest of the map is obtained by replication of this rectangle.

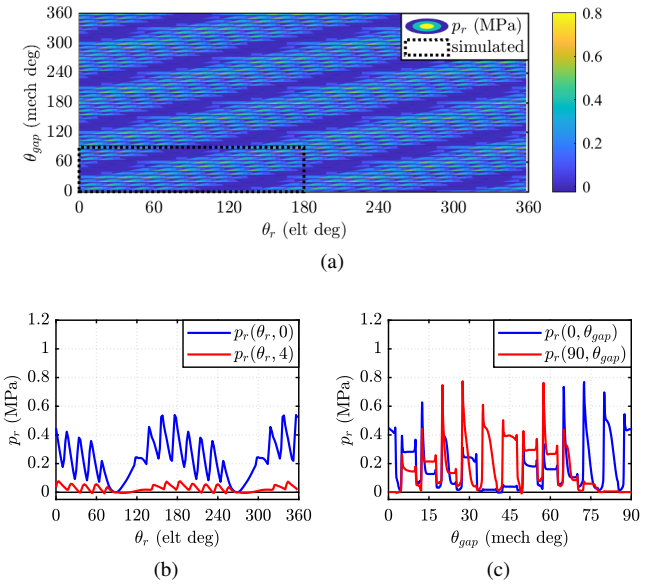

Fig. 7. Radial magnetic pressure at the airgap for the DW-IPM motor in the T_{max} operating point: a) magnetic pressure map, b) magnetic pressure waveform function of the rotor position and c) magnetic pressure waveform along the airgap.

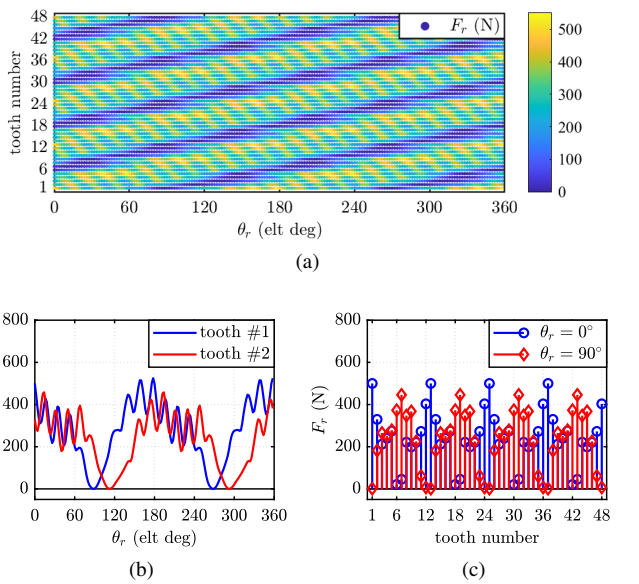

Fig. 8. Tooth radial force for the DW-IPM motor in the T_{max} operating point: a) tooth radial force function of the rotor position and the tooth number, b) radial force waveform function of the rotor position and c) radial force waveform along the airgap.

A simulation of the complete motor and full electric period rotation is performed to validate the extension result. The two axes of this plot represents the rotor position θ_r (expressed in electrical degrees) and the airgap coordinate θ_{gap}, expressed in mechanical degrees. The horizontal yellow lines (index of low magnetic pressures), appear at the slot opening, where the magnetic field is lower. To better understand this plot, additional waveform are extracted from the pressure map and reported in Fig. 7.

The first two waveform extracted are reported in Fig. 7b and show the radial magnetic pressure function of the rotor position and for two given airgap coordinates (selected at one tooth and one slot opening). These two waveform are obtained by extracting two different horizontal lines from the pressure map of Fig. 7a. It is worth noting that there are two main harmonic components, the second harmonic (because of the two poles in one period) and the 20^{th} harmonic, related to the number of equivalent rotor slots (i.e. the edges of the flux barriers). Dealing with the pressure value in the two selected points, the level of magnetic pressure over one tooth (blue line) is higher than the magnetic pressure over the slot opening (red line), as expected. Moreover, the magnetic pressure on the slot opening not null, because of the flux leakage path. A similar analysis is performed in the other pressure map direction, and it is reported in Fig. 7c. There, the magnetic pressure is reported function of the airgap coordinate, for two rotor positions. This is equivalent to extract vertical lines from the pressure maps and just 90 mechanical degrees are plotted here for clarity. The slot opening are clearly visible in this plot, since the magnetic pressure is almost zero in that area and these holes in the waveform are static with the rotor position. While, the rotor rotation is visible in this framework from the peak value of the magnetic pressure, that is shifted in space.

After the FEA simulations and the related post-processing, the torque waveform over one electrical period is computed, as well as the radial and tangential tooth forces for each stator tooth and for the rotor rotation of one electrical period. As example, Fig. 8 reports the radial tooth force map for the T_{max} point of the DW-IPM motor.

Please, note this map is in a discrete form along the y-axis: each horizontal line represent the force on one stator tooth, function of the rotor position. To better understand how the map is built, the first two lines (representing the first two tooth) are extracted and plotted in Fig. 8b. Here is evident that the force acting on one tooth is very similar to the force acting on the other teeth, with a delay, due to the angular displacement between the two teeth. Dealing with the harmonic content, the comments done for the radial pressure hold, with the main harmonics orders related to the poles (second harmonic) and the number of barrier edges (20^{th} for this motor). Fig. 8c shows the radial force of all the stator tooth for two different rotor positions and it is equivalent to extract two separate columns from the force map shown in Fig. 8a. The two selected rotor positions have half period delay, and it is evident that the peak force moves among the tooth, as a periodic waveform sampled from the stator tooth.

B. Torque ripple comparison

The first quantity that is studied is the torque waveform in the five operating points reported in Fig. 4. The torque waveform and the torque ripple FFT are reported in Fig. 9 for the two benchmark motors. Besides the torque ripple amplitude (coherent with the previous analysis), and the fact that all the torque harmonic are multiple of 6 (as expected

for three-phase motors) this simulation highlights also the deep differences in the spectra of the two machines. The DW-IPM motor presents in general lower values of torque ripple, but at higher frequency compared to the CW-SPM motor. This difference has two main sources: the winding configuration and the rotor structure. Dealing with the winding configuration, the distributed winding typically induces the slot harmonic, related to the number of slots per pole pair n_s, that for this motor is 24. Indeed, the 24^{th} harmonic (in the electric angle domain) is the main harmonic for most of the operating points. On the other side, the concentrated winding induce the 6^{th} harmonic and all the multiples. On the rotor side, the two motors are quite different: for DW-IPM machine, the 4-barrier design is adopted, with an equivalent number of rotor slots per pole pair equal to 20. This is obtained with a correct placement of the flux barriers edges and the torque ripple harmonic is the closest multiple of 6 to this number (i.e. 18^{th} harmonic order), while the magnet of the CW-SPM motor induces all the even harmonic orders. Another critical behavior, that makes the NVH analysis complex is the fact that the amplitude of each harmonic order change with both torque and speed. This happens because, above the base speed, the operating point in the (i_d, i_q) domain change, changing the local magnetic behaviors of the motor, as shown in Fig. 5.

C. Tooth forces comparison

The comparison is extended to the forces acting on the stator tooth of the two motors. The first tooth force considered is the radial force and the forces of the first tooth and their FFT are reported in Fig. 10 for the 5 operating points and the two reference machines.

Besides the amplitude difference, due to the different number of tooth (y axis limits are 10 times bigger for the CW-SPM motor), there are some other details between the two motors that can be critical for NVH performance. First of all, the radial force for the DW-IPM motor increase with the flux linkage (i.e. with torque and no field weakening), while is almost constant for the CW-SPM motor. This is probably due to the magnetic properties of the two machines: for the former, the rotor is mainly magnetized from the q-axis stator current, while the latter relies mainly on the PM flux linkage to magnetize the motor, that is not variable with load. A second crucial difference for the NVH analysis is the harmonic content of the two machines. The DW-IPM motor presents higher harmonic content (18^{th} and 20^{th} electrical order harmonics), related to the equivalent rotor slotting. These high-order harmonics are null for the CW-SPM motor, playing a crucial role in the high-speed analysis, as will be demonstrated later. Furthermore, the amplitudes of each harmonic order change with the speed, as happens for torque ripple. Another interesting feature, related to the type of winding, is the fact that for DW, the radial forces became null for 2 times at electrical period, while this is not true for the CW winding. This features is caused by the different periodicity of the stator and rotor: for DW there are an integer number of slots for one rotor pole, while this is not true for the CW arrangement.

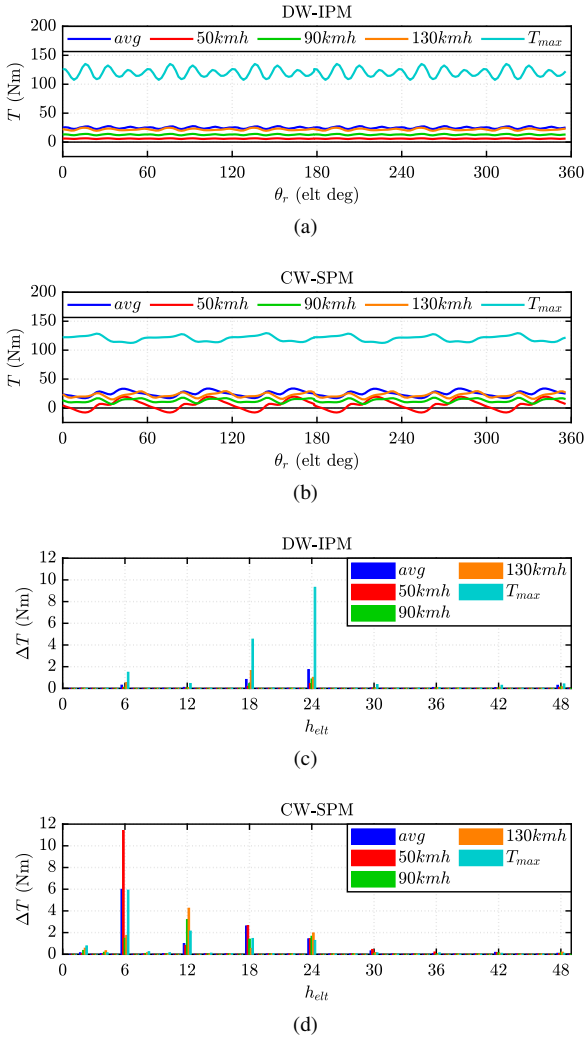

Fig. 9. Torque ripple details on the selected operating points: torque waveform function of the rotor position and torque ripple FFT.

The tooth force analysis is performed also in the tangential direction. The results (waveform for one tooth function of the rotor position and FFT) are reported in Fig. 11 for the two motors and the 5 operating points. The comments done for torque ripple and tooth radial force are still valid for the tangential forces. The tangential force spectra is even more critical than the radial force spectra, because of the higher variation of the components with load. Furthermore, in the spectra of the tangential forces of the DW-IPM motor, the relative amplitude of the slot harmonics (18^{th} and 20^{th} harmonic) is higher compared to the radial force spectra and the CW-SPM motor, with possible side effects on the NVH performance.

V. NVH Analysis of the Powertrain

Romax Spectrum allows conducting dynamic analysis on the complete e-powertrain model considering the main e-NVH sources by importing the electromagnetic forces (radial and tangential) acting on the single stator tooth and the torque ripple as a function of the angular coordinate for different

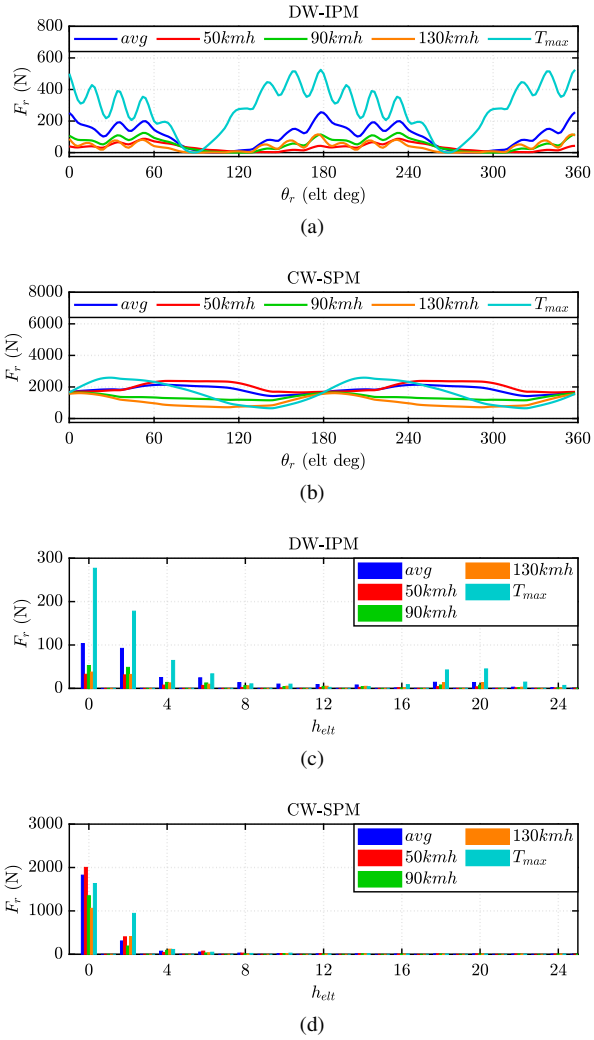

Fig. 10. Tooth radial forces waveform function of rotor position and its FFT for the two motors in the selected operating points.

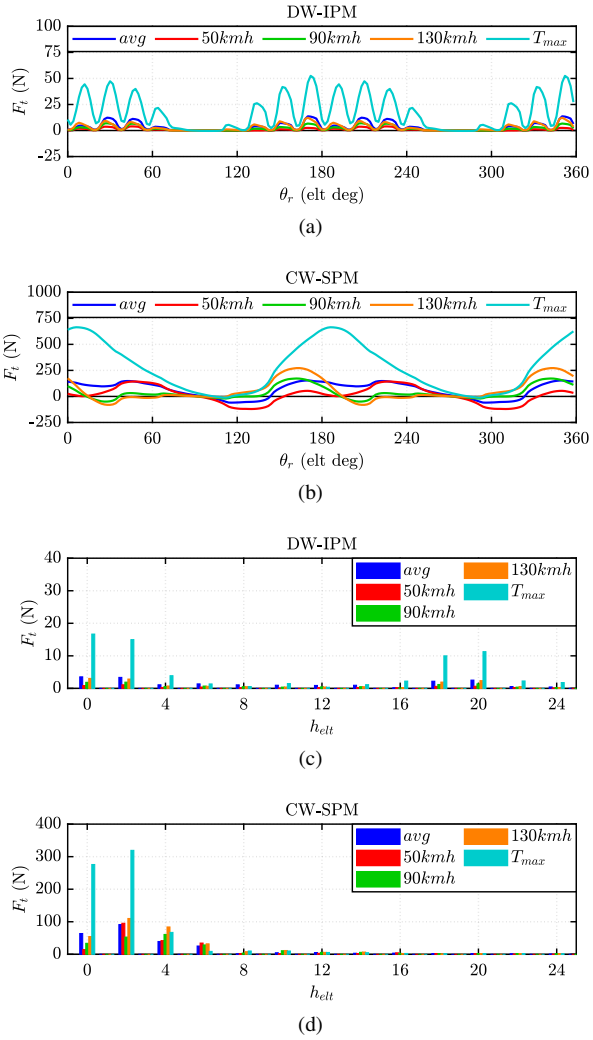

Fig. 11. Tooth tangential forces waveform function of rotor position and its FFT for the two motors in the selected operating points.

operating speeds of the e-motor. The forces to the FEM stator model are applied to the tooth surface using a weighted RBE3 connection. Weighted RBE3 calculates weightings for each node such that a stator tooth deflection will apply a uniform pressure over all element faces which are made up of connected nodes [9]. The torque ripple is applied on the rotor shaft. The result that is selected as NVH index is the Equivalent Radiated Power (ERP), computed from vibroacoustic analysis, that takes place at a fixed torque over the entire speed range.

The results of the acoustic analysis in terms of ERP are reported in Fig.12. The results are reported for a 25 Nm load case and the whole range of speed, while for the *50kmh*, *90kmh* and *130kmh* points the specific speed and torque conditions were considered. For the analysis of this load case, the results are an interpolation of the response of 5 working points with different speeds in the range. The harmonics with the greatest response have been selected and shown in the graph.

Analyzing the results, the CW-SPM motor has an acoustic response stronger than the DW-IPM, especially at low rotation speeds, where the difference in maximum ERP amplitude is up to 2 orders of magnitude. On the other hand, at high rotor speeds, the two motors seem to emit a similar sound power level. Furthermore, for the DW-IPM motor, it is the 24^{th} harmonic relating to the number of slots per pole pair which has a predominant contribution over the others and shows a peak in the acoustic response around 9000 RPM, probably due to some resonances in the system, which require deeper investigations. On the contrary, in the CW-SPM motor the prevailing harmonics are those of lower order, in particular the 6^{th} has a greater contribution than all the others up to 8000 RPM, then the 2^{nd} prevails at high rotation speeds.

The differences in ERP performance between the two motors can be explained as a combination of several effects: on the one hand, the CW-SPM motor, which presents a greater acoustic response compared to the DW-IPM at medium-low speeds, has tooth forces of one order larger due to the concentration on a smaller number of teeth. However, the

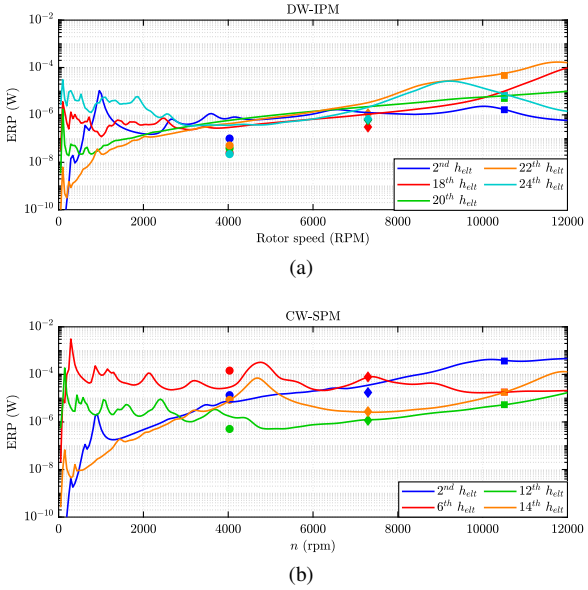

Fig. 12. Equivalent Radiated Power (ERP): ERP curves calculated at 25 Nm for selected harmonic orders with markers referring to the selected operating points. a) DW-IPM machine. b) CW-SPM machine.

size of the teeth is also different, being longer but also wider than those of the DW-IPM motor. Furthermore, in the CW-SPM motor, as we have seen in the previous paragraphs, the harmonics of the electromagnetic forces are concentrated in the lower orders and these excite the mechanical structure at lower frequencies, compared to the DW-IPM motor. This can be critical because the mechanical system acts as a low-pass filter, attenuating higher-order harmonics but less effectively filtering out low-frequency excitation.

VI. Conclusions

In this paper, a process for the analysis of the e-NVH performance of an electric vehicle powertrain is presented and the computational steps to obtain the e-NVH sources is reviewed. The effect of the different motor structures (a 4-layer IPM motor with distributed winding and a SPM motor with concentrated winding) is considered both at flux maps level and at torque-speed map level, including the related optimal control trajectories. Then, the harmonic content of the two machines is compared in terms of torque ripple and tooth forces, highlighting the differences of the two motors. The DW-IPM solution presents, in general lower torque ripple and forces amplitude, associated to higher harmonic orders, while the CW-SPM motor presents higher harmonic amplitudes at lower orders. These differences in terms of e-NVH sources are compared at e-powertrain system level using ERP indicators. The analysis highlights that the CW-SPM motor produces in general more noise, especially at low speeds, because of the lower harmonic order involved, while for higher speeds (above 8000 rpm), the two motors preform in a similar way as far as the ERP index is concerned. These differences between the two motor, due to the combination of multiple effects, highlight the need to combine classic e-motor design tools with advanced simulation tools in the design of electrified propulsion systems capable of predicting the combined system behavior.

Acknowledgment

This study was carried out within the MOST – Sustainable Mobility Center and received funding from the European Union Next-GenerationEU (PIANO NAZIONALE DI RIPRESA E RESILIENZA (PNRR) – MISSIONE 4 COMPONENTE 2, INVESTIMENTO 1.4 – D.D. 1033 17/06/2022, CN00000023). This manuscript reflects only the authors' views and opinions, neither the European Union nor the European Commission can be considered responsible for them.

The research has been conducted with the support of Power Electronics Innovation Center (PEIC) of Politecnico di Torino.

References

[1] M. R. Raia, S. Ciceo, F. Chauvicourt, and C. Martis, "Asymmetric stator slot opening geometry for pmsm nvh optimisation," in *IECON 2023-49th Annual Conference of the IEEE Industrial Electronics Society*, 2023, pp. 1–6.

[2] J. Cederlund, S. Nategh, and D. Lennström, "Topology optimization of electrical machines for nvh purposes in e-mobility applications - part 1," in *IECON 2021 – 47th Annual Conference of the IEEE Industrial Electronics Society*, 2021, pp. 1–6.

[3] T. Bertoncello, G. Franceschini, B. Raghuraman, M. Diana, and A. Lidbeck, "Unsymmetrical pole design vs skewing for improving nvh characteristics and performance of high speed pmsm electric machines," in *IECON 2022 – 48th Annual Conference of the IEEE Industrial Electronics Society*, 2022, pp. 1–6.

[4] M. Michon, R. Holehouse, A. Shahaj, H. Jafarali, and al., "System Interactions Affecting NVH Performance of an Electric Vehicle Drivetrain," *SAE Technical Paper 2019-01-1545, 2019*.

[5] Y. Jia, D. Yue, and Q. Meng, "Nvh performance optimization for pure electric vehicles," in *2023 5th International Conference on Robotics and Computer Vision (ICRCV)*, 2023, pp. 259–265.

[6] S. Feng and R. Qu, "Nvh analysis of integrated motor and two-speed gearbox system for electric vehicles," in *2022 International Conference on Electrical Machines (ICEM)*, 2022, pp. 115–121.

[7] G. Pellegrino, A. Vagati, P. Guglielmi, and B. Boazzo, "Performance comparison between surface-mounted and interior pm motor drives for electric vehicle application," *IEEE Transactions on Industrial Electronics*, vol. 59, no. 2, pp. 803–811, 2012.

[8] C. Lu, S. Ferrari, and G. Pellegrino, "Two design procedures for pm synchronous machines for electric powertrains," *IEEE Transactions on Transportation Electrification*, vol. 3, no. 1, pp. 98–107, 2017.

[9] "Hexagon romax." [Online]. Available: https://hexagon.com/products/product-groups/computer-aided-engineering-software/romax

[10] Hexagon, "NVH7: Electric Machine Modelling and NVH Analysis." [Online]. Available: https://nexus.hexagon.com/documentationcenter/it-IT/bundle/romax_DT_2023.1_Tutorials/page/132877392.html

[11] S. Ferrari, G. Pellegrino, and et al., "SyR-e: Synchronous Reluctance (machines) - evolution." [Online]. Available: www.github.com/SyR-e/syre_public

[12] S. Ferrari, P. Ragazzo, G. Dilevrano, and G. Pellegrino, "Flux and loss map based evaluation of the efficiency map of synchronous machines," *IEEE Transactions on Industry Applications*, vol. 59, no. 2, pp. 1500–1509, 2023.

[13] D. Meeker, "FEMM: Finite Element Method Magnetics." [Online]. Available: www.femm.info